



CHARA TECHNICAL REPORT

No. 87 5 April 2002

Visibility Measurements from Fringe Amplitudes Using Mathcad with Application to Upsilon Andromedae

H.A. McAlister

ABSTRACT: In response to the accumulation of the first substantial collection of observational data from the CHARA Array, obtained during the fall of 2001, a series of Mathcad programs has been developed as a means for reducing these data to calibrated visibilities. The Mathcad tools developed to date include routines that calculate estimated visibilities for single and double stars, ephemerides from binary star orbital elements, (u,v) plane and projected baseline coverage for target stars, and the analysis of an observational dataset to yield a mean value of raw visibility. This Technical Report describes the last of these programs and presents the results from a set of data obtained during the night of 6 Nov 2001 for the extrasolar planetary system Upsilon Andromedae.

1. INTRODUCTION

This report complements TR (Theo's draft), which considers the determination of visibility through the analysis of fringe power spectra. As we obtain an understanding of our data and the performance of the Array, it seems wise to develop more than one route for data analysis, and the effort described here has focused on the more straightforward relation between fringe amplitude and visibility. Mathcad was selected as an alternative to CHARA's usual use of C or IDL mostly because of the author's inexperience with those languages but also because of the intuitive nature of Mathcad and its usefulness in teaching interferometric data reduction in graduate level courses.

This discussion is based upon the paper by Benson *et al.* (1995) and assumes the detection scheme shown in Figure 1 wherein two detectors look at opposite sides of a beam splitter

* Center for High Angular Resolution Astronomy, Georgia State University, Atlanta, GA 30303, USA
Tel: (404) 651-2932, Fax: (404) 651-1389, Anon FTP: chara.gsu.edu, website: www.chara.gsu.edu/CHARA

within which interference arises from beams input from a pair of telescopes whose path length difference has been zeroed. The notation used by Benson *et al.* (1995) is adopted here for ease of reference back to that paper.

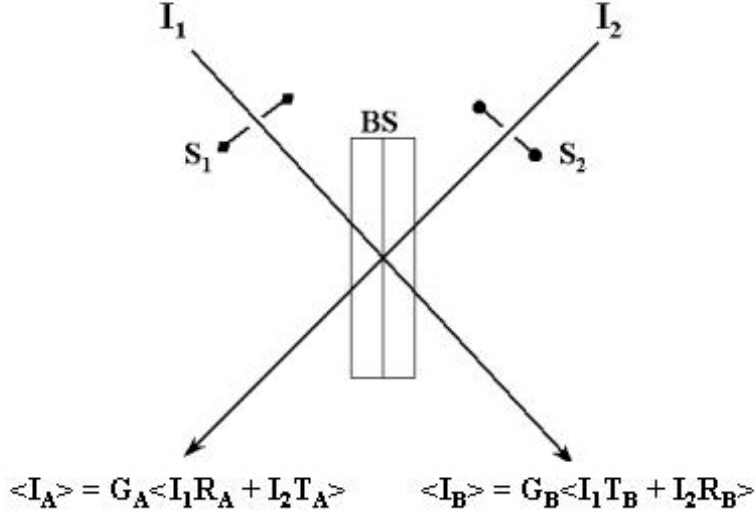


Fig.1 – Beam splitter combination geometry showing input and output beams with calibration shutters

As one scans through the zero path condition, presently done using a piezo-driven dither mirror, the detectors on the A and B sides of the beam splitter see average signals related to the average reflected R and transmitted T components of the input beams multiplied by a detection gain factor G. The shutters at S₁ and S₂ are used to close either or both inputs to determine the bias (or “dark”) level of the detector and to permit determination of the reflection and transmission efficiencies as described below.

As in Benson *et al.* (1995), we define the following: I₁ and I₂ are the input intensities of the beams to be combined (not directly measured in CHARA’s present configuration); *r* and *t* are the complex reflection and transmission coefficients for the beam splitter; R and T are the squared moduli of those coefficients; σ is the wave number (1/λ); *x* is the path difference between the two beams; φ is a phase error arising from instrumental and atmospheric effects; and V is the visibility. Note from Figure 1 that R and T are not assumed to be the same in the two channels A and B. By normalizing each of the two detected signals to its average, the detection gain factors divide out, and one is left with normalized interferograms I_A and I_B given by:

$$I_A(x) = 1 + \{[2V(I_1 I_2)^{0.5} |r_A| |t_A|] / [I_1 |r_A|^2 + I_2 |t_A|^2]\} \text{sinc}(\pi \Delta \sigma x) \cos(2\pi \sigma_\phi x + \phi) \quad (1)$$

and

$$I_B(x) = 1 - \{[2V(I_1 I_2)^{0.5} |r_B| |t_B|] / [I_1 |t_B|^2 + I_2 |r_B|^2]\} \text{sinc}(\pi \Delta \sigma x) \cos(2\pi \sigma_\phi x + \phi). \quad (2)$$

Note the transposition of the beam splitter efficiencies *r* and *t* in the divisors, which arose from the normalization process. In the rest of this analysis, we assume that the sinc and cosine factors are unity at *x* = 0, which is where we measure the peak amplitude of the fringe.

FRINGE AMPLITUDE VISIBILITIES

Of course, the quantity ϕ leads to a statistical fluctuation in the cosine factor making it always less than 1. Effects contributing to ϕ include random path length variations arising from instrumental instabilities and variations in the effective air paths that together create piston error. There are also degrading effects arising from our current restriction to manual fringe tracking as well as from telescope tracking errors that lead to loss of image overlap.

The practice of observing “calibration” stars of known visibility before and after the “target” star is assumed to correct for atmospheric and instrumental effects, but it would not compensate for losses in visibility due to guiding and fringe tracking errors if those effects are not randomly insinuating themselves into the data.

At the zero path difference (the fringe center), equations (1) and (2) simplify to:

$$I_A(x) = 1 + 2V(I_1 I_2)^{0.5} |r_A| |t_A| / (I_1 |r_A|^2 + I_2 |t_A|^2) \quad (3)$$

and

$$I_B(x) = 1 - 2V(I_1 I_2)^{0.5} |r_B| |t_B| / (I_1 |t_B|^2 + I_2 |r_B|^2) . \quad (4)$$

Defining the quantities $\alpha = I_2/I_1$ and $\beta_{A,B} = |r_{A,B}|^2/|t_{A,B}|^2 = R_{A,B}/T_{A,B}$, equations (3) and (4) can be rewritten as:

$$I_A(x) = 1 + 2V(\alpha\beta_A)^{0.5} / (\alpha + \beta_A) \quad (5)$$

and

$$I_B(x) = 1 - 2V(\alpha\beta_B)^{0.5} / (1 + \alpha\beta_B) . \quad (6)$$

The divisors in the A and B channel interferograms are not of the same form, a fact that might be missed in a casual reading of Benson *et al.* (1995). In any case, the ratios α and $\beta_{A,B}$ are close to 1. Taking the difference between equations (5) and (6) yields:

$$I_A(x) - I_B(x) = 2V[(\alpha\beta_A)^{0.5}/(\alpha + \beta_A) + (\alpha\beta_B)^{0.5}/(1 + \alpha\beta_B)] \quad (7)$$

which is rewritten

$$V = 0.5[I_A(x) - I_B(x)] [(\alpha\beta_A)^{0.5}/(\alpha + \beta_A) + (\alpha\beta_B)^{0.5}/(1 + \alpha\beta_B)]^{-1} \quad (8)$$

or

$$V = 0.5\Gamma[I_A(x) - I_B(x)] \quad (9)$$

where

$$\Gamma = [(\alpha\beta_A)^{0.5}/(\alpha + \beta_A) + (\alpha\beta_B)^{0.5}/(1 + \alpha\beta_B)]^{-1} . \quad (10)$$

The factor Γ would be unity in the ideal case of $\alpha = \beta_{A,B} = 1$. In the actual case of imbalanced beams and unequal transmission and reflection efficiencies, the placement of shutters in the beam combiner as indicated in Figure 1 provides a means for determining combinations of the ratios α and $\beta_{A,B}$ and evaluating Γ . Inspection of Figure 1 shows that when shutter S_1 is closed, the average signal reaching detector A, indicated as I_{AS1} , is $G_A I_2 T_A$ while that reaching B, I_{BS1} , is $G_B I_2 R_B$. Similarly, when S_2 is closed, $I_{AS2} = G_A I_1 R_A$ and $I_{BS2} = G_B I_1 T_B$. Thus, we can use these shuttered signal levels to calculate the following quantities:

$$\gamma_B = \alpha\beta_B = (I_2 / I_1)(R_B / T_B) = I_{BS1} / I_{BS2} , \quad (11)$$

and

$$\gamma_A = \beta_A / \alpha = (I_1 / I_2)(R_A / T_A) = I_{AS2} / I_{AS1} . \quad (12)$$

Notice that the gains of the two channels divide out. Substituting these relations back into equation 10 provides the working equation into which we can insert the factors $\gamma_{A,B}$ determined from the shuttered signal levels detected by the A and B channels:

$$\Gamma = [(\gamma_A)^{0.5} / (1 + \gamma_A) + (\gamma_B)^{0.5} / (1 + \gamma_B)]^{-1} . \quad (13)$$

The A and B sides of the beam splitter can separately processed in which case equations (5) and (6) can be rewritten as:

$$I_A(x) = 1 + [2V\gamma_A^{0.5} / (1 + \gamma_A)] \quad (14)$$

and

$$I_B(x) = 1 + [2V\gamma_B^{0.5} / (1 + \gamma_B)] . \quad (14)$$

The practice at the beginning and end of each observation sequence is to alternately close S_1 , then both S_1 and S_2 , then S_2 , thereby providing information to evaluate equation (13). Figure 2 shows as an example the observing sequence as recorded on side A of the beam splitter for a data set taken for the star HR 409 on the night of 6 Nov 2001. In this particular data sequence, it is obvious that the quantity α/β is close to 1. The color difference between the target star and its calibrator is probably the largest factor in determining whether it is important to explicitly determine α and β . It is certainly straightforward to do so as long as the shuttered signal levels are recorded. For the data reduced here, Γ was always within 1% of 0.5.

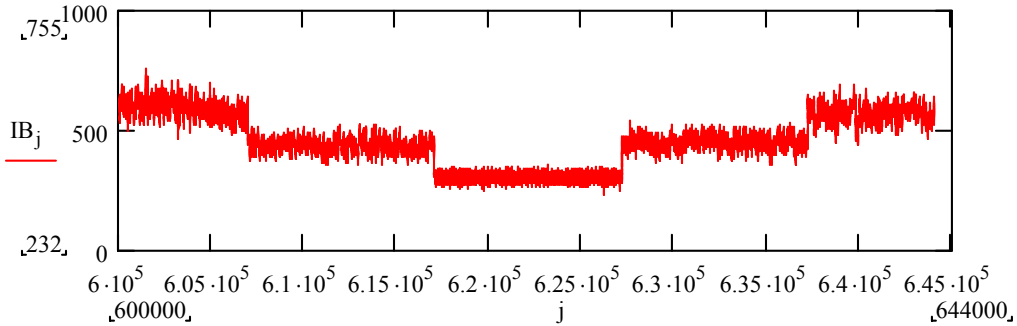


Fig2 – Shutter data obtained at the beginning of a data sequence. Steps are in milliseconds of time.

2. STEPS IN DATA PROCESSING

Data sets obtained during the fall of 2001 generally consist of ten-minute accumulations of scans, in millisecond time steps, with shuttering sequences at the beginning and end. The first step in the processing is to manually locate the shuttering sequences and to calculate values averaged over 5,000 samples for I_{AS1} , I_{AS2} , I_{BS1} , I_{BS2} and the bias levels at the beginning and end of the data set. These values are then used to calculate the ratios α and β and the multiplicative factor Γ .

The program then uses the dither mirror position information, recorded in microns for each sample, to locate the beginning and ending of a dither mirror scan at a “safe” distance beyond the S_2 shutter data and to slice the data set into arrays with each row comprising a single scan. Ten-minute data sets typically yield 650 scans each consisting of 837 samples. Each scan is padded at the beginning and end with the average scan value to ensure that scans of 1024 samples are available for fast Fourier processing. Examples of simultaneous scans recorded on the A and B sides of the beam splitter are shown in Figure 3.

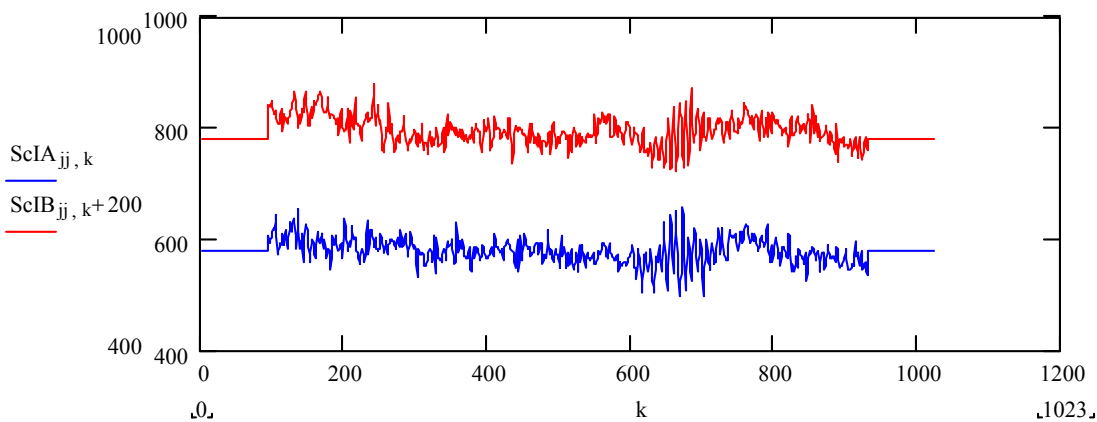


Fig 3. Raw A and B scans, with B offset for clarity, are shown. The fringe packet late in the scan is apparent.

FFTs are then taken of each scan for the purpose of applying a low-pass filter in which all components of the transform are zeroed beyond 15 Hz. The inverted low-pass filtered scans then provide smoothed versions of each scan for the purpose of normalization. Figure 4 shows such a smoothed scan superimposed on the raw, unfiltered version.

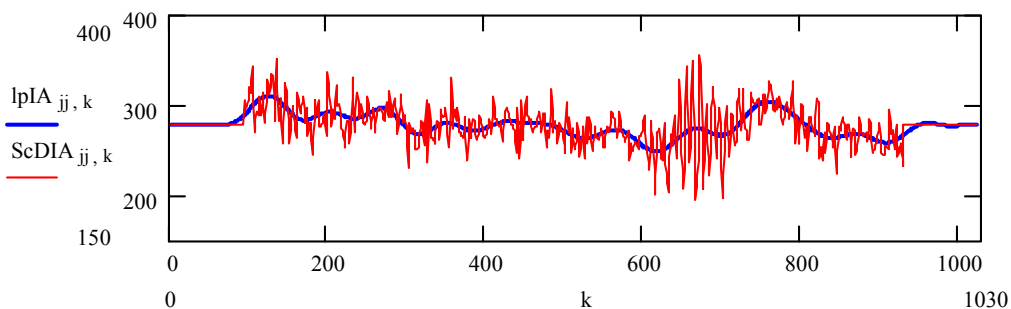


Fig 4. A raw scan containing the high-frequency fringe information is shown superimposed on its low-pass filtered version just prior to normalization.

The bias value, which remained within 1% of 300 counts for all the data reduced here, is next subtracted from each A and B scan, and vector division with respect to its low-pass filtered version normalizes each scan. Figure 5 shows the result of normalizing the scan in Figure 4.

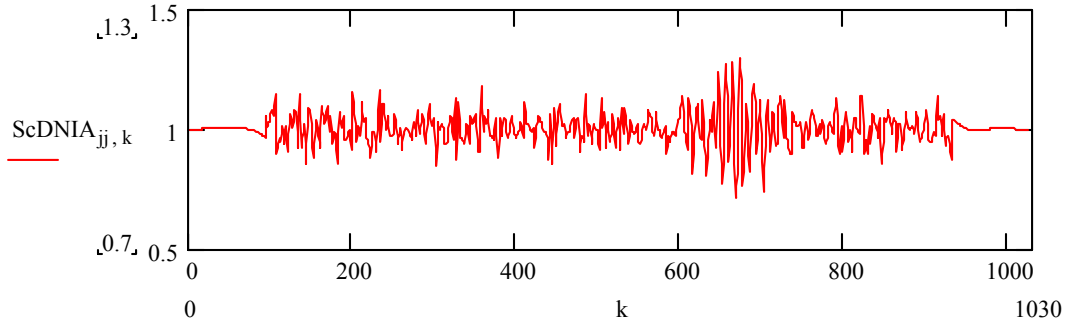


Fig 5. The scan shown in Figure 4 has been normalized to its low-pass filtered version.

At this point, the differences between the normalized A and B scans are calculated and adopted as defining “visibility scans” according to equation (9) whose amplitudes will be extracted as representations of V . The visibility scan determined by combining the normalized B scan with it’s A partner from Figure 5 is shown in Figure 6.

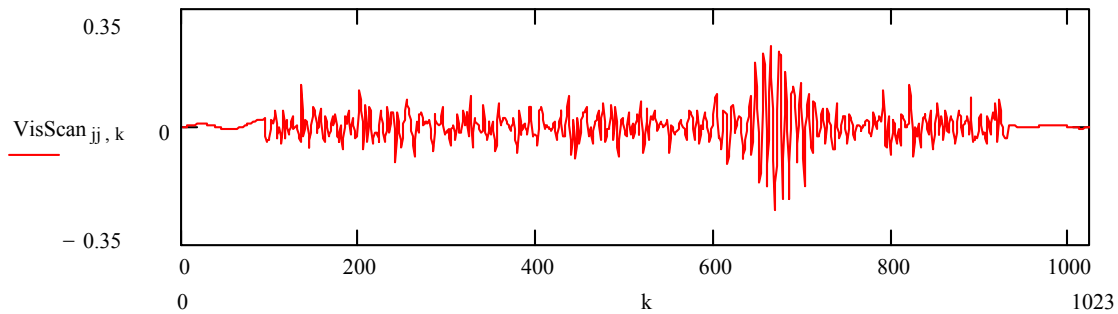


Fig 6. The “visibility scan”, a realization of Equation (9), is shown after combining the normalized scan in Figure 5 with the simultaneously observed and normalized B scan.

The next step is to band-pass filter each visibility scan in a frequency regime surrounding the expected fringe frequency. This is accomplished by Fourier transforming the visibility scans, suppressing all frequencies lower than 70 Hz to one-fifth their values, locating the peak in the power spectrum and keeping only those components within 25 Hz of the peak. (In the data set used as the example here, the average bandpass center of the peak was 108.4 Hz with an rms variation of 13.1 Hz.) This filtering step suppresses the high frequency noise fluctuations that would otherwise significantly bias the estimate of the fringe amplitude and suppresses a persistent component around 60 Hz.

FRINGE AMPLITUDE VISIBILITIES

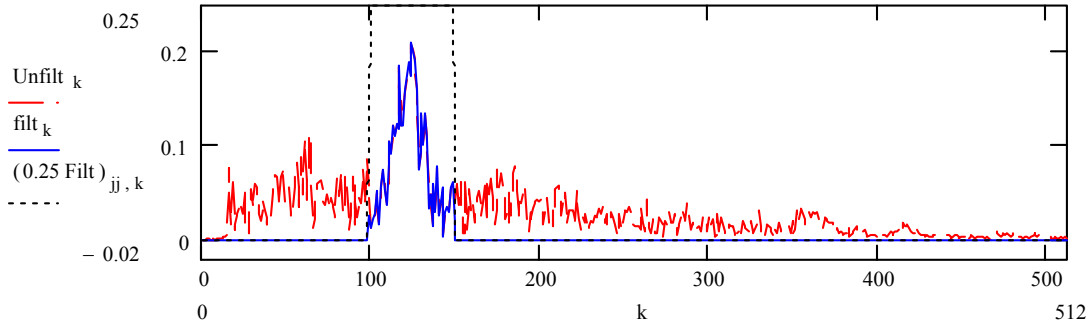


Fig 7. The filtered region of the power spectrum, centered upon the fringe peak, is shown with power in the frequencies outside this region set to zero.

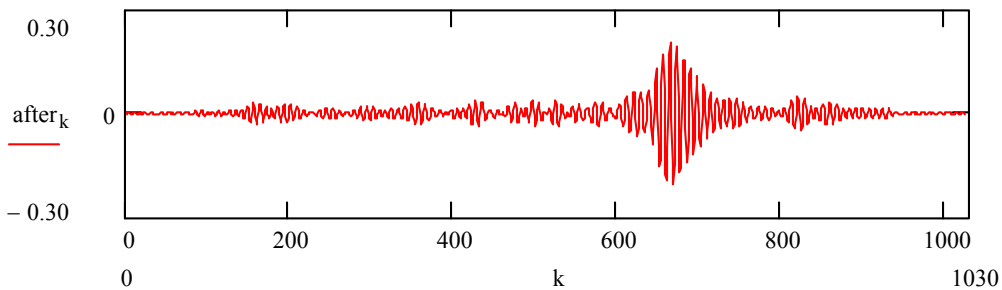


Fig 8. The resulting band-pass filtered visibility scan is shown above.

Figure 7 shows the band-pass filtering applied to the power spectrum of the visibility scan developed in the earlier figures while Figure 8 shows the resulting smoothed visibility scan after inversion of the band-pass filtered power spectrum. Figure 9 shows the band-pass filtered fringe packet more clearly.

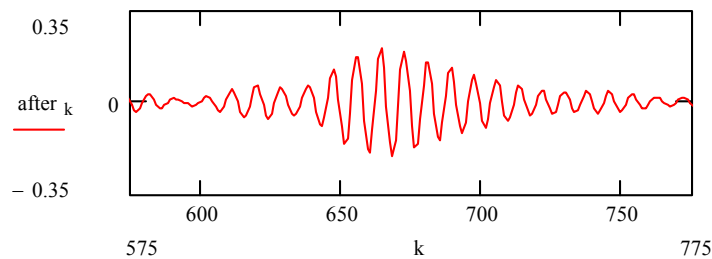


Fig 9. A higher resolution view of the fringe packet in Fig. 8 is shown.

The processing thus far yields hundreds of visibility scans, each of which is next inspected for its maximum deviation from zero. Those deviations are then the estimates of fringe visibility. The visibility estimates provided by a 10-minute scan are inspected in histogram form, keeping odd and even numbered estimates separate in case there are systematic differences resulting from differences in the forward and backward throw of the dither mirror. (The properties of the dither mirror are currently being measured using a laser interferometer.) The histograms then provide final estimates of the visibility, still uncalibrated against a star of known visibility. In the 17 datasets involving υ Andromedae described below, The variation between backward and forward throws of the dither mirror, resulting in even and odd numbered scans, showed a

mean value of $-0.6 \pm 3.6\%$. Thus, we will not further discriminate in this analysis between scans of opposite directions. An example histogram is shown in Figure 10.

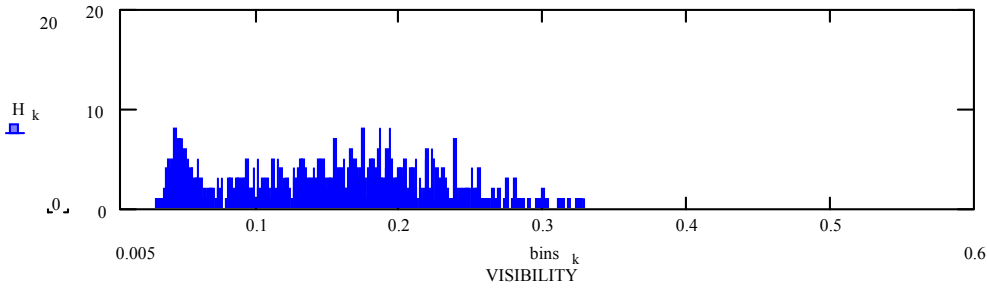


Fig 10. A histogram of visibilities resulting from 658 scans is shown.

The example dataset was selected because it contains a gap of about 1.5 minutes in the 10-minute series in which fringes are lost, presumably due to a drift of the zero path location beyond the range of the dither mirror. This is not a typical situation, but illustrates a problem that arises in attempts to discard scans considered to be bad. The algorithm developed here will still locate the highest intensity peak in the expected region of the power spectrum containing a fringe and will produce a “false” fringe from which it measures a visibility. Those false fringes are invariably of low amplitude, hence the large bump at the low visibility end of Figure 10. The individual visibility measurements are plotted in Figure 11 in which the false fringes are clearly seen. The two values with zero visibility, located just after $k = 350$ in Figure 11, are the result of an adjustable signal-to-noise evaluator that sets V to zero for fringes whose amplitudes are less than some multiple of the rms fluctuations in the background (measured away from the fringe packet). In this case, the criterion was set to a SNR of 1. Figures 12 and 13 show the result of increasing the threshold to 3 and then to 7, at which point the middle region of these data containing false fringes is well captured but other random real fringes of low SNR are also eliminated.

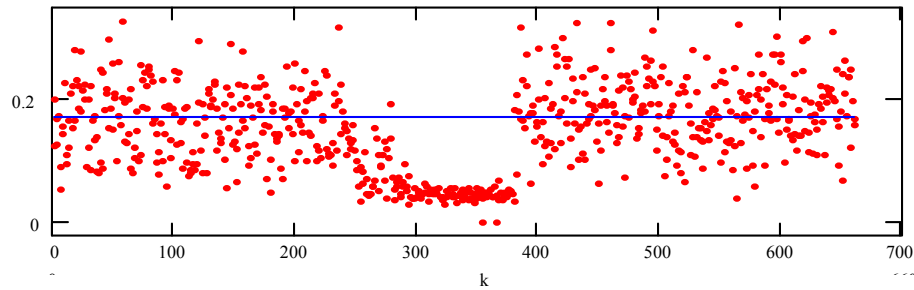


Fig 11. 658 visibilities during a 10-minute sequence, with fringe loss midway through the sequence, are shown. The blue line is the mean visibility measured after the dropouts have been ignored.

FRINGE AMPLITUDE VISIBILITIES

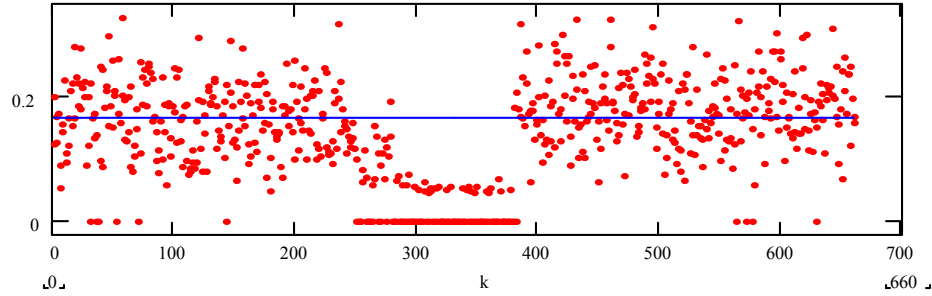


Fig 12. Setting a signal-to-noise threshold of 3 captures many, but not all, of the spurious fringe detections.

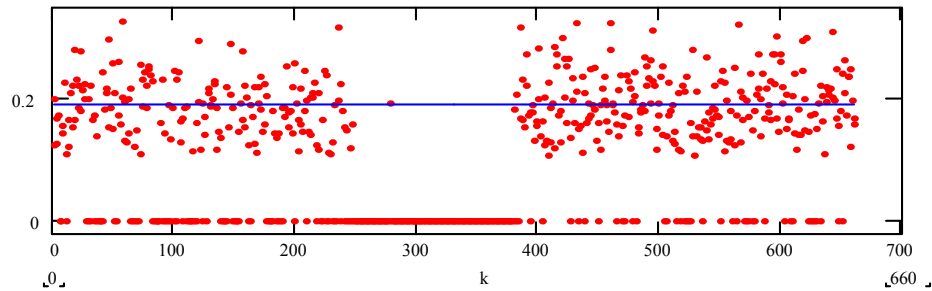


Fig 13. A SNR threshold of 7 captures most of the dropouts but also depletes low SNR fringes randomly.

Another way to visualize these data is shown in Figure 14 in which 1-minute averages of visibility are displayed with error bars representing the rms deviations from the mean. The region of fringe loss clearly stands out in the two subsets of low visibility. The line through the points represents the average of the other 1-minute series after the two obviously flawed time segments have been “switched” off. These one-minute averages are useful in detecting possible high time-frequency visibility variations that would arise from a “wide” stellar companion scanned by the changing baseline projection during a 10-minute observing sequence that would otherwise be lost in lumping the data into a single measurement.

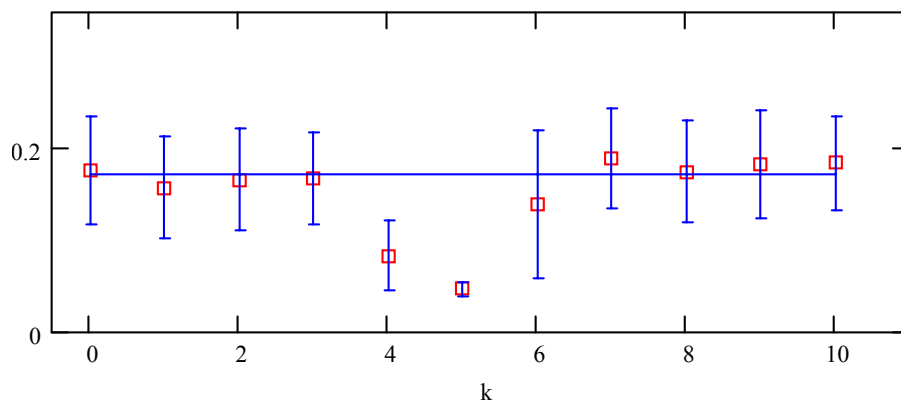


Fig 14. One-minute subsets of the data from Fig. 11 are shown.

The use of a thresholding criterion in an attempt to deselect “false” fringes is clearly dangerous. For the data set displayed here, increasing the threshold to a SNR of 3 does indeed catch most of the dropouts during the fifth and sixth minutes, but it also will randomly deselect

real fringes whose amplitudes are low because of the statistical nature of the actual fringe distribution. By eliminating those fringes from the mean value, a bias towards higher visibility will result. And, because one cannot be assured that the de-selection will be applied to the same fractional parts of the distributions for the program and calibrator stars, the calibration process will not eliminate this bias. It is therefore appropriate to correct for lost fringes by deleting blocks of data from the analysis rather than attempt to locate false fringes with an unsophisticated statistical argument.

Determining the mean visibility can be viewed as a process of centroiding on a histogram. The mean values of V for 1-minute integrations shown in Figure 12 have error bars that might be regarded as the half-widths of the histograms of each integration. The variations of these means from their overall mean value, shown as the horizontal line in Figure 12, are indicative of the precisions of the fits and are used here as the estimator of the error of the raw visibility determination. For the example used here, the data set yields $V = 0.183 \pm 0.008$.

The Mathcad routine described by this report is available from the author. The reduction of a 10-minute data set requires about 45 seconds on a 500 MHz pc with 512Mb of RAM. About half that time is involved in reading in the input data file, typically 25 Mb in size.

3. APPLICATION TO UPSILON ANDROMEDAE

There remains the possibility that the sample of extrasolar planetary systems discovered to date is contaminated by face-on binary star systems which yield planetary masses for the secondary when an actual $\sin i$ of nearly zero is assumed to be near unity. Long-baseline interferometry provides new resolution leverage that can cull the sample of face-on binaries. One simple means for examining these stars is to let the baseline scan the object during the course of a night during which time the visibility will vary due to changing baseline projection. This technique was applied by Boden et al. (1998) to 51 Pegasi for which they found no evidence for a stellar companion.

The star υ Andromedae (HR 458 = HD 9826, $\alpha = 01\ 36\ 47.8$, $\delta = +41\ 24\ 20$, $V = +4.09$, Sp. Type = F8V, $\pi = 74.3 \pm 0.7$ mas) is accompanied by three extrasolar planets having periods of 4.6, 242 and 1269 days (Butler et al. 1999, Stepinski et al. 2000). Abt (1976) reported a companion with a period of 198 days, a result that is now generally regarded as spurious. Two wide companions are listed in the Washington Double Star catalog, but they are regarded as being optical rather than physical in nature.

As a pilot for a more extensive forthcoming survey of accessible extrasolar planetary systems, we observed υ And on the night of 6 Nov 2001 interlaced between observations of a calibrator star HR 409 (HD 8671, $\alpha = 01\ 26\ 18.54$, $\delta = +43\ 27\ 28$, $V = +5.96$, Sp. Type = F7V, $\pi = 24.2 \pm 0.7$ mas), 2.8° from υ And. The results of those observations are presented in Table 1.

FRINGE AMPLITUDE VISIBILITIES

Table 1. Observations of υ And and Calibrator														
Object	U_{beg}	V_{beg}	R_{beg}	θ_{beg}	U_{end}	V_{end}	R_{end}	θ_{end}	LST	Alt	V_{raw}	σ_{Vraw}	V_{cal}	σ_{Vcal}
HR 409	-58.73	324.79	330.06	-10.25	-66.43	323.19	329.95	-11.61	-0.03	70.6	0.242	0.011	-	-
υ And	173.54	273.24	323.69	32.42	168.00	277.92	324.75	31.15	0.42	74.2	0.106	0.009	0.497	0.054
HR 409	-92.11	316.24	329.38	-16.24	-97.98	314.27	329.19	-17.32	1.09	79.9	0.171	0.015	-	-
υ And	136.16	298.86	328.42	24.49	129.13	302.46	328.87	23.12	1.37	82.3	0.071	0.006	0.457	0.052
HR 409	182.43	261.84	319.13	34.87	177.37	267.03	320.56	33.59	1.67	80.4	0.139	0.009	-	-
υ And	107.37	311.85	329.82	19.00	99.47	314.68	330.03	17.54	1.99	81.6	0.066	0.005	0.409	0.042
HR 409	140.82	292.64	324.76	25.70	134.08	298.43	327.17	24.19	2.21	77.1	0.177	0.012	-	-
υ And	81.86	320.05	330.35	14.35	73.29	322.22	330.45	12.81	2.49	77.4	0.089	0.008	0.446	0.048
HR 409	114.38	307.93	328.49	20.38	107.06	310.91	328.83	19.00	2.74	72.3	0.220	0.011	-	-
υ And	47.00	327.25	330.61	8.17	38.94	328.33	330.63	6.76	3.13	70.7	0.064	0.003	0.340	0.024
HR 409	87.29	317.74	329.52	15.36	77.85	320.42	329.74	13.66	3.47	64.7	0.161	0.009	-	-
υ And	12.96	330.41	330.66	2.25	4.45	330.63	330.66	0.77	3.74	64.0	0.070	0.004	0.460	0.035
HR 409	59.11	324.71	330.05	10.32	51.06	326.17	330.14	8.90	4.10	~55	0.140	0.006	-	-
υ And	-26.60	329.58	330.65	-4.61	-35.02	328.78	330.64	-6.08	4.44	56.1	0.055	0.003	0.366	0.029
HR 409	18.35	329.83	330.34	3.18	10.32	330.19	330.36	1.79	4.84	49.9	0.163	0.012	-	-
υ And	-63.92	324.29	330.53	-11.15	-71.21	322.71	330.47	-12.44	5.11	48.6	0.061	0.004	0.333	0.033
HR 409	-21.29	329.64	330.33	-3.70	-21.29	329.64	330.33	-3.70	5.47	43.1	0.210	0.017	-	-

The (U,V) values are given in terms of the projected baseline lengths at the beginning and end of each of the 10-minute observation sets and were calculated from a Mathcad program developed for CHARA by Anders Jerkstrand. The projected baseline lengths R and position angles θ are also given along with the local sidereal time at the beginning of each ten-minute observation sequence and the beginning altitude of the star. The observing log for that night indicates that transparency was decreasing during the last third of the pointings. The zenith distance was also beginning to be significant. These effects clearly show themselves in the average intensity levels of the data, which dropped by a factor of two from start to finish.

Figure 15 presents the raw and calibrated visibilities for υ And and its reference star. Clearly, the photosphere of υ And is more resolved than that of HR 409. The calibrated values for υ And were determined by linear interpolation of reference visibilities, shown as diamonds without error bars in the middle curve. Conditions were changing significantly during the course of this night, and there is no guarantee that a linear interpolation is very meaningful. Furthermore, it should be pointed out that the one-minute samplings within each ten-minute dataset are quite steady and show no significant slopes. This leads to the troubling conclusion that the large variation in raw visibility is instrumental in nature. The two raw visibility curves in Figure 1 track each other fairly well, suggesting a continuous change in this effect. It would be very worthwhile to spend a part of one night taking short (5 minutes) data sets on the same object separated by small slews of the telescopes and delay lines to an offset location and then immediately returning to the star. This will shed light on whether the variations we see here in the raw visibility of the calibrator star are continuous and amenable to linear interpolation.

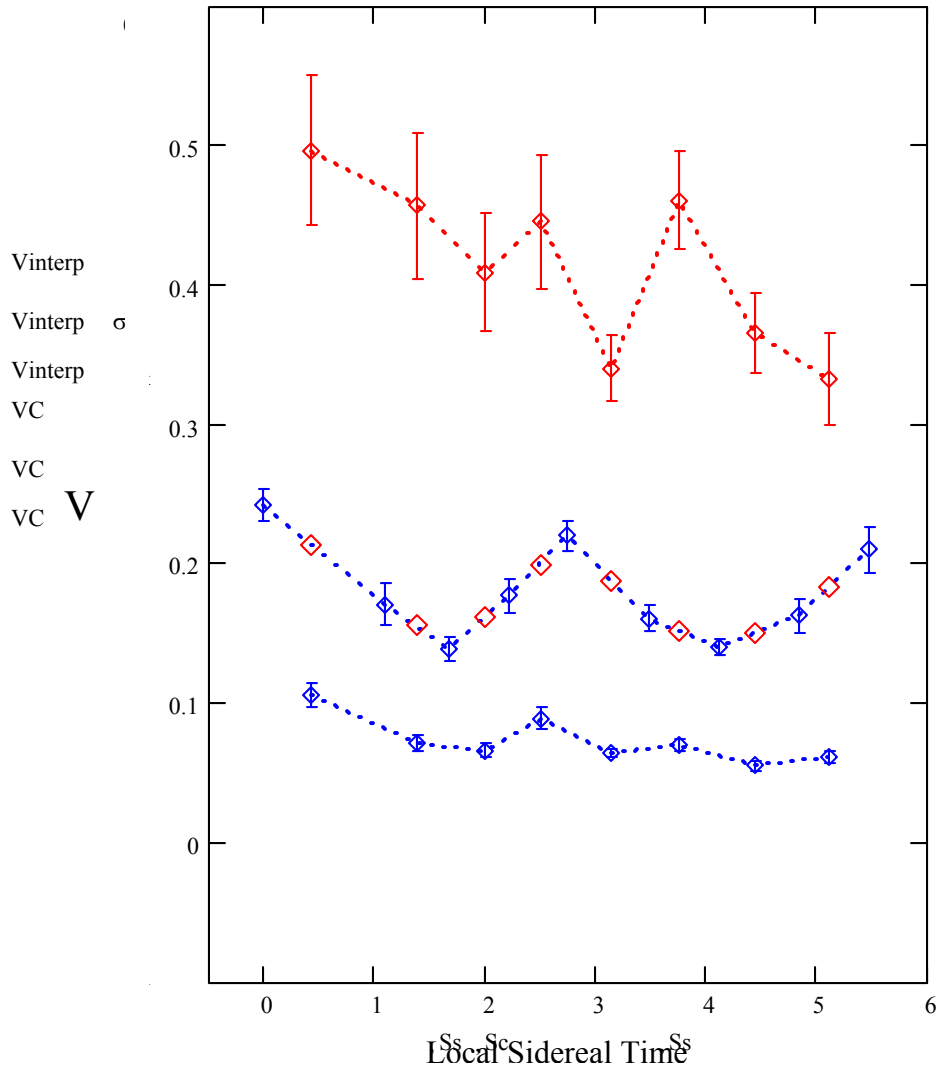


Fig 15. Raw and calibrated visibilities for v And and HR 409 are shown above.

As mentioned earlier, Theo ten Brummelaar is independently developing a data pipeline based upon estimating visibilities from the power spectra of fringes. Figure 16 shows a comparison of his results (diamonds) with those produced here from fringe amplitudes (squares). While the results are generally in good agreement, especially for the first half of the night, there is a systematic offset that is prominent in the second half of the night. These two approaches should give identical results, and we will continue to explore the nature of this disagreement. It is at least heartening that we are not wildly in disagreement.

FRINGE AMPLITUDE VISIBILITIES

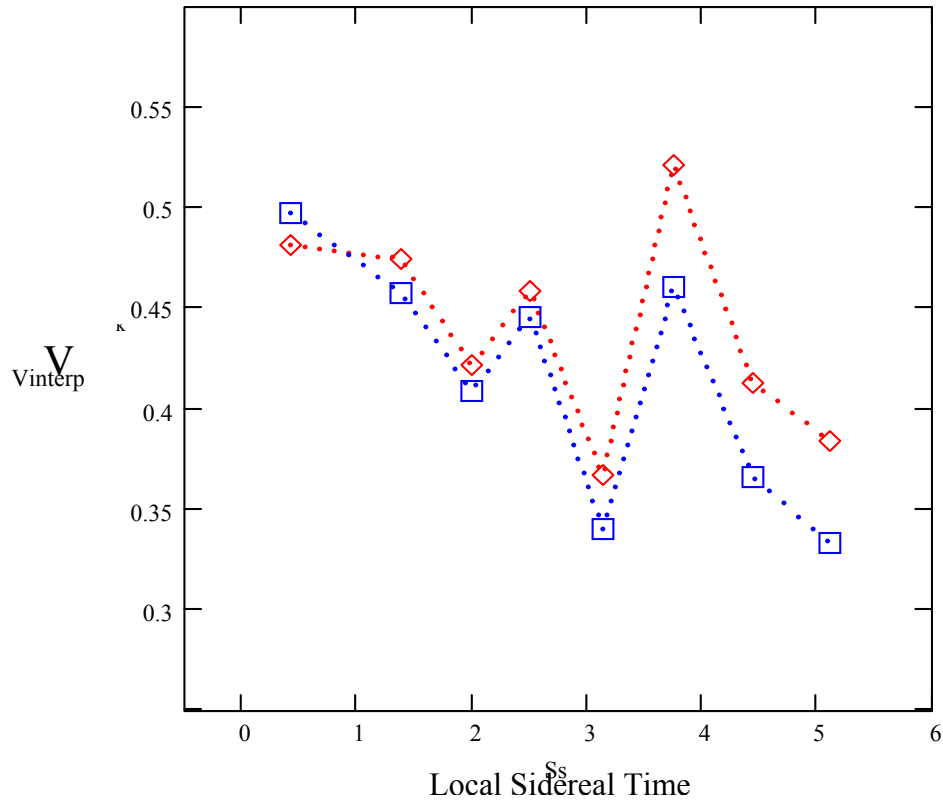


Fig 16. A comparison between results from fringe amplitude (blue square) and fringe power spectra (red diamonds) is shown above.

One can use trigonometric parallaxes and estimated linear diameters, the latter assigned according to MV type from Cox (2000), of the two stars to calculate expected visibilities. This leads to a value of $V = 0.955$ for the calibrator and $V = 0.65$ for υ And. The final calibrated visibilities, now adjusted for the expected value of the calibrator, are plotted against projected baseline in Figure 17. The solid nearly linear curve is the calculated visibility based upon the Hipparcos parallax of 74.25 mas. The dashed curve is the visibility resulting from a parallax based upon the spectral type, yielding an angular diameter of 1.18 mas. There is no reason to accept the spectroscopic parallax over the trigonometric value, but it turns out that υ And is about half a magnitude brighter than expected for its spectral type if the Hipparcos parallax is correct. With the uncertainties in our calibration process, no conclusions are reached regarding the variations in V with baseline. While this particular night of data does not yet serve the purpose of inspecting this extrasolar planetary system for stellar companions, it has been very useful in the development of reduction tools and the exploration of calibration procedures.

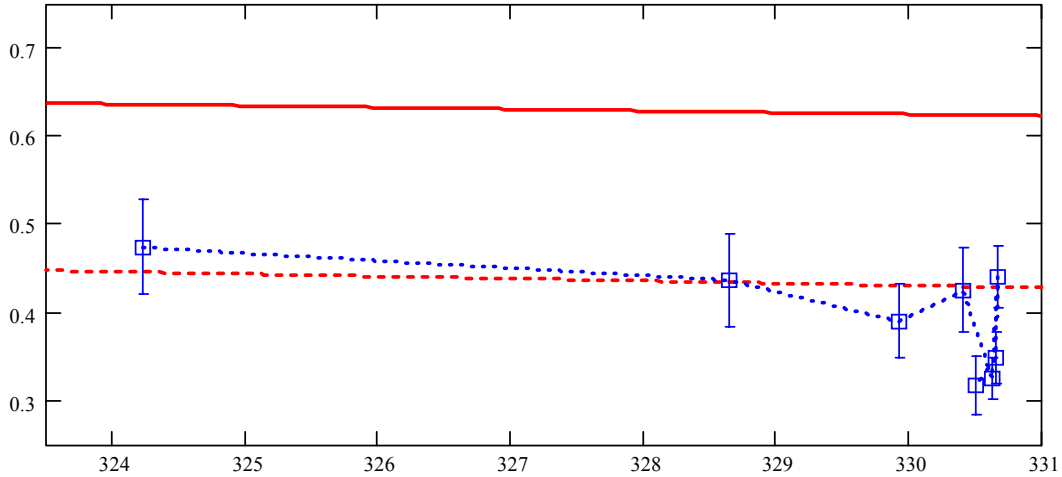


Fig 17. The calibrated visibilities for υ And are plotted above against projected baseline along with two estimates of the anticipated visibility.

Finally, if we regard the spread in the data as being representative of the error of the measurements, then we can fit uniform disk visibility curves to these data to derive a value for the angular diameter of υ And. Such a graphical fit is shown in Figure 18 for which the mean

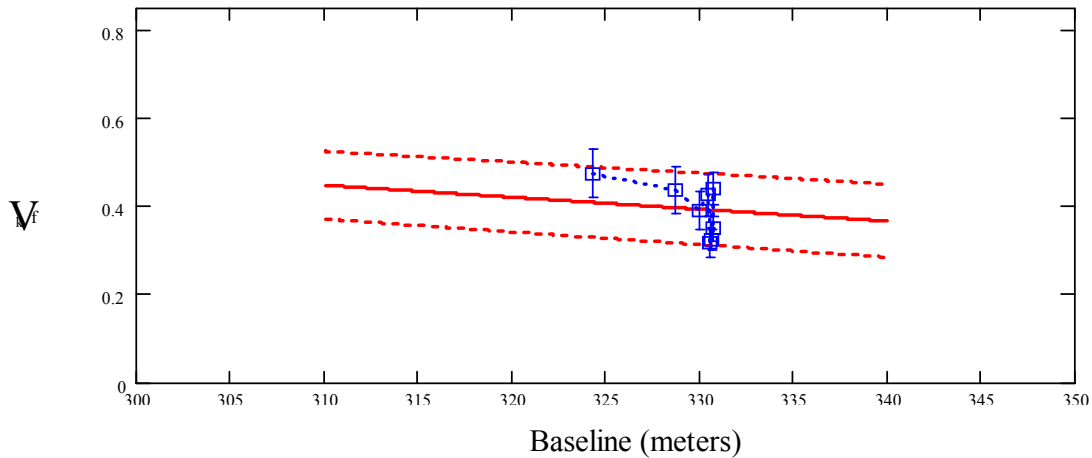


Fig 18. The data for υ And are well represented by a diameter of 1.1 ± 0.1 mas angular diameter is 1.1 ± 0.1 mas. If this result is accurate, then υ And is about 35% larger than expected for a F8V star at the Hipparcos distance. However, this diameter is consistent with the spectroscopic parallax for this star.

4. REFERENCES

Abt, H.A. and Levy, S.G., **The Astrophysical Journal Supplement**, **30**, 273, 1976.

Benson, J.A., Dyck, H.M. and Howell, R.R., **Applied Optics**, **34**, 51, 1995.

FRINGE AMPLITUDE VISIBILITIES

Boden, A.F., Van Belle, G.T., Colavita, M.M, Dumont, P.J., Gubler, J., Koresko, C.D., Kulkarni, S.R., Lane, B.F., Mobley, D.W., Shao, M. and Wallace, J.K., **The Astrophysical Journal**, **504**, 39, 1998.

Butler, R.P., Marcy, G.W., Fischer, D.A., Brown, T.M., Contos, A.R., Korzennik, S.G., Nisenson, P. and Noyes, R.W., **The Astrophysical Journal**, **526**, 916, 1999.

Cox, A.N., **ASTROPHYSICAL QUANTITIES**, 4th Edition, (Springer-Verlag: New York), p. 389, 2000.

Stepinski, T.F. Malhotra, R. and Black, D.C., **The Astrophysical Journal**, **545**, 1044, 2000.